Chemical Science

ROYAL SOCIETY OF CHEMISTRY

EDGE ARTICLE

View Article Online
View Journal | View Issue

Cite this: *Chem. Sci.*, 2025, **16**, 11487

All publication charges for this article have been paid for by the Royal Society of Chemistry

The color-tuning mechanism in multi-resonance thermally activated delayed fluorescence emitters: site effects in peripheral modification and skeleton fusion†

Zicong Situ,[a] Xingqing Li,[a] Shengsheng Wei,[a] Xiang Wang,[b] Yang Li,[a] Yan Wan,[c] Lian Duan,*[b] Andong Xia *[a] and Zhuoran Kuang *[a]

Ultra-narrowband, highly modifiable multi-resonance thermally activated delayed fluorescence (MR-TADF) materials are critical for high-performance, wide-color-gamut display applications, yet balancing broad color tunability while maintaining high color purity remains challenging. We present a proof-of-concept study into 7,10-di-*tert*-butyl-5-mesityl-5*H*-benzo[5,6][1,4]azaborinin-o[3,2,1 *jk*]carbazole (**BIC**) derivatives with a B/N MR skeleton to elucidate the site effects of peripheral modification and skeleton fusion on MR-TADF properties. Incorporating electron donating groups (EDGs) in a *meta*-(N–π–N) configuration forms D–void–A motifs, which retain or even enhance the MR characteristics, achieving a blue-shifted emission. In contrast, EDG modifications in a *para*-(N–π–N) configuration result in conjugative D–π–A motifs, leading to a red-shift in emission. Rigid skeleton fusion in an extended D–π–A motif compensates for the potential increase in vibronic coupling, which typically arises from a decline in MR properties. Furthermore, the centrosymmetric fused skeleton suppresses the excited-state structural relaxation in dielectric environments, achieving narrowband green emission (528 nm, 30 nm or 929 cm^{-1} in emission FWHM). This work elucidates the intrinsic mechanism of the widely applicable site effects in regulating MR characteristics and color-tuning *via* peripheral modification and skeleton fusion, providing a theoretical foundation for the design of ultrapure long-wavelength emission MR-TADF materials.

Received 4th March 2025
Accepted 19th May 2025

DOI: 10.1039/d5sc01751c

rsc.li/chemical-science

Introduction

Multi-resonance thermally activated delayed fluorescence (MR-TADF) materials based on rigid polycyclic aromatic frameworks show extraordinary sharp emission spectra owing to the inherent structural vibration inhibition and electronic transition characteristics.[1–7] Due to their outstanding advantage of high color purity, MR-TADF materials have been extensively used in organic light-emitting diodes (OLEDs) with high-definition displays.[8] To date, boron/nitrogen (B/N)-embedded polycyclic aromatic hydrocarbons (PAHs) have been proven to be the most recognized multiple-resonance (MR) skeletons, and the MR effect manifests in short-range charge-transfer (SRCT) transitions between the atomically separated lowest unoccupied molecular orbital (LUMO) and highest occupied molecular orbital (HOMO) in boron and nitrogen atoms, respectively, which was first reported by the Hatakeyama group called **DABNA-1** (Fig. 1).[1]

To improve the luminescence performance and achieve full-color tuning, a series of highly efficient MR-TADF emitters have been designed by introducing and amplifying the influence of peripheral units attached to the *para* site of the B-substituted phenyl ring in the MR-core (*i.e.* **TBN-TPA**, **CzBN3**, **DtCzB-DPTRZ**, *etc.*).[9–11] The incorporation of peripheral modification units with electron donating groups (EDGs) and electron withdrawing groups (EWGs) significantly narrows the energy gap and improve the emission oscillator strength (*f*), leading to a bathochromic shift in emission and increased radiative rates, without significantly compromising color purity (*i.e.* narrowband emission characteristics were maintained).[12–16] The incorporation of an asymmetrically fused carbazole with extended π-conjugation introduces an additional *para*-(N–π–N) configuration, which not only further red-shifts the emission but also helps maintain narrowband emission for high color

[a]*State Key Laboratory of Information Photonic and Optical Communications, School of Science, Beijing University of Posts and Telecommunications (BUPT), Beijing 100876, P. R. China. E-mail: andongxia@bupt.edu.cn; kuang@bupt.edu.cn*

[b]*Key Laboratory of Organic Optoelectronics & Molecular Engineering of Ministry of Education, Department of Chemistry, Tsinghua University, Beijing 100084, P. R. China. E-mail: duanl@mail.tsinghua.edu.cn*

[c]*College of Chemistry, Beijing Normal University, Beijing 100875, P. R. China*

† Electronic supplementary information (ESI) available: Materials and methods, supplementary stationary and transient absorption spectra, spectral global analysis and TD-DFT calculations. See DOI: https://doi.org/10.1039/d5sc01751c

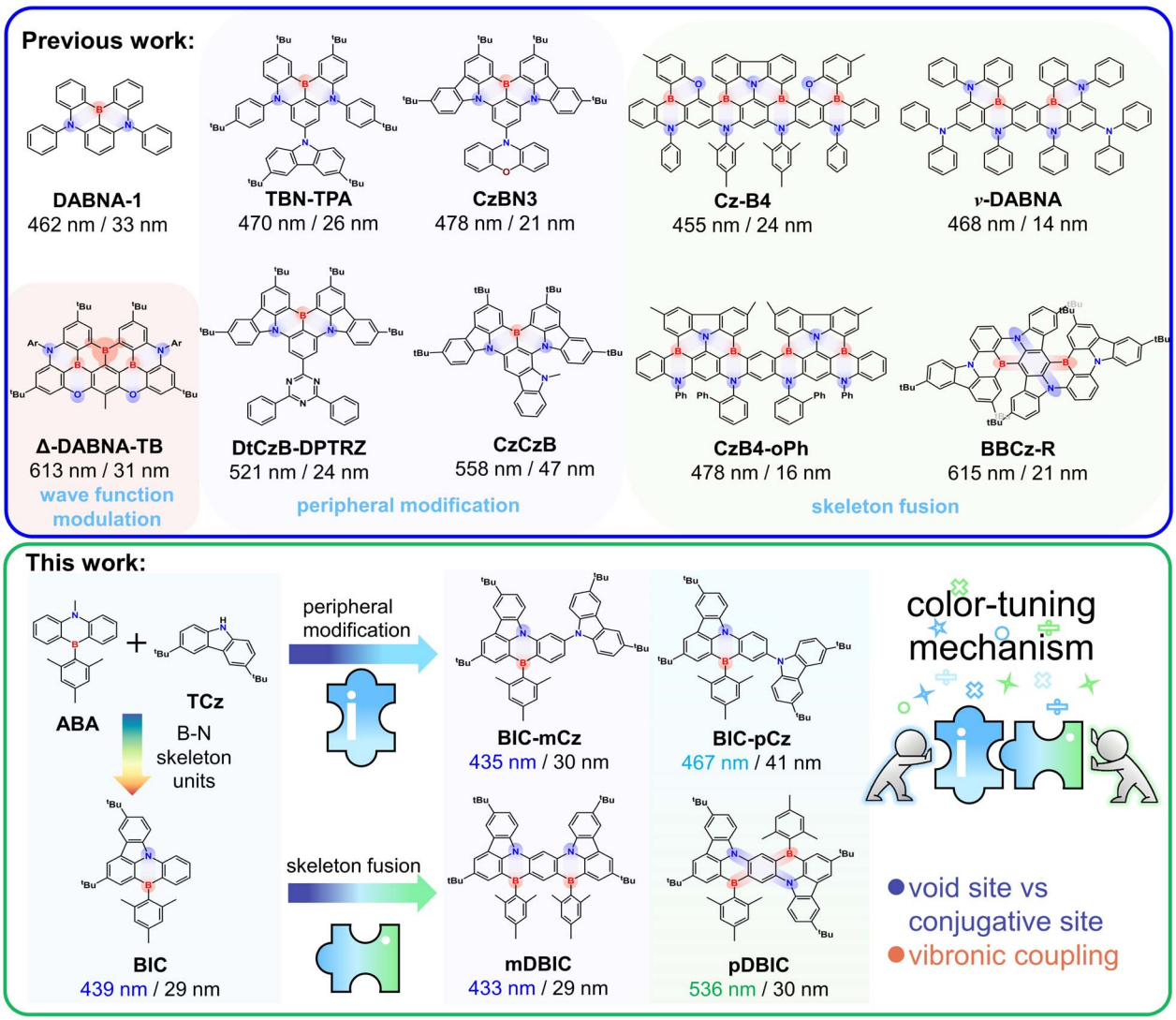

Fig. 1 Schematic representation of the molecular designs and proof-of-concept models discussed in this work.

purity, as demonstrated in emitters such as **CzCzB** and **BNTPA**.[17,18] Furthermore, MR-TADF emitters designed by conjugating and fusing multiple B/N skeleton units with *meta*- or *para*-(N–π–N) conjugations have achieved ultra-narrow emission and full-tuning (*i.e.* **CzB4**, ***ν*-DABNA**, **CzB4-*o*Ph**, **BBCz-R**, *etc.*).[19–23] Significant efforts have been made to modify B/N-skeleton-based MR-TADF emitters for color tuning[20,24,25] and explore the underlying physical mechanism.

Color tuning through chemical modification of the B/N skeleton can typically be categorized into two main strategies: (i) peripheral modification by substituting bulky donor/acceptor (D/A) groups, which introduce long-range charge-transfer (LRCT) characteristics,[26–31] and (ii) fusing D/A fragments into the rigid PAH framework to extend the π-conjugation.[32–37] Since the LUMO and HOMO are offset by one atom in MR skeletons, the wave function of frontier orbitals becomes very sensitive to the site of peripheral modification and skeleton fusion, eventually leading to significant change in photophysical properties (*i.e.* **Δ-DABNA-TB**).[38] Therefore, when modifying the B/N skeleton for color tuning purposes, it is crucial to consider the effectiveness of the modification sites. The primary consideration is controlling the lowest emission state energy, *i.e.*, inducing red or blue shifts, which are typically linked to how skeleton modifications influence the π-electronic conjugation.[14,30,39] Ensuring that the unique narrowband emission characteristics of MR-TADF materials are preserved after the modification is equally important. Achieving this often involves a trade-off between changes in MR characteristics and various factors, such as vibronic coupling, skeleton flexibility, excited-state structural relaxation, *etc.*[40–46] However, the physical mechanism underlying full-color regulation of MR-TADF emitters through peripheral modification and skeleton fusion remains incompletely understood.

We previously reported wide-range color-tuning MR-TADF frameworks, 7,10-di-*tert*-butyl-5-mesityl-5*H* benzo[5,6][1,4] azaborinin-o[3,2,1-*jk*]carbazole (**BIC**), composed of 9-methyl-10-mesityl-9,10-dihydro-9-aza-10-boraanthracene (**ABA**) and 3,6-di-*tert*-butylcarbazole (**TCz**) (Fig. 1).[47] **BIC-mCz** and **BIC-pCz** were

obtained by introducing **TCz** on the **BIC** core with *meta*- and *para*-(N–π–N) configurations, respectively. **mDBIC** (*meta*-(N–π–N) conjugation) and **pDBIC** (*para*-(N–π–N) conjugation) were obtained by conjugatively fusing dual BIC moieties with mirror symmetric and centrosymmetric geometries, respectively. In this study, we utilize the above two sets of peripheral modification and skeleton fusion isomers as proof-of-concept models to comprehensively demonstrate the impact of the modification site on MR-TADF color tuning. Through quantum chemical calculation and time-resolved spectroscopy, we focus on examining how the following factors influence color regulation: (1) conjugative and non-conjugative connection in peripheral modification and skeleton fusion, (2) the detrimental effect of conjugative skeletal expansion on MR properties, (3) the trade-off between SRCT and LRCT characteristics in the lowest emissive state, (4) vibronic coupling during emission transitions, and (5) skeleton flexibility and excited-state structural rearrangement.

Results and discussion

Basic photophysics

Fig. 2 presents the stationary absorption and the emission spectra of **BIC** and its derivatives. The **BIC** core displays a narrow absorption band centered at 408 nm, which is attributed to the ^{1}SRCT absorption with MR properties. Upon peripheral modification with **TCz** (an EDG) in a *meta*-(N–π–N) configuration, as seen in **BIC-mCz**, a new broad absorption band emerges at around 390 nm, corresponding to the ^{1}LRCT absorption (see the simulated UV-vis absorption spectra in Fig. S1† and the corresponding electronic excitation analysis). Notably, **BIC-mCz** retains the sharp ^{1}SRCT absorption characteristics of the **BIC** core. A similar trend is observed in **mDBIC**, where the fusion of **TCz** in a *meta*-(N–π–N) configuration within the **BIC** skeleton leads to analogous spectral changes. In contrast, **BIC-pCz** and **pDBIC**, which feature peripheral modification and skeleton fusion of **TCz** in a *para*-(N–π–N) configuration, respectively, exhibit distinct shifts in the lowest absorption band. **BIC-pCz** exhibits a broadening of its lowest absorption band, attributed to the introduction of a low-energy ^{1}LRCT transition. Meanwhile, **pDBIC** maintains narrowband characteristics, but its lowest absorption band shifts to approximately 510 nm.

Upon interrogating the emission spectra (Fig. 2b), both **BIC-mCz** and **mDBIC** in toluene retain the narrowband properties of the **BIC** core, with a slight blueshift to 435 and 433 nm, respectively (see Table S1† for detailed photophysical parameters). In contrast, **BIC-pCz** exhibits a noticeable redshift and broadening emission (λ_{em} = 467 nm, PL FWHM = 41 nm or 1806 cm^{-1}) compared to the **BIC** core (λ_{em} = 439 nm, PL FWHM = 29 nm or 1482 cm^{-1}). This suggests that the MR features in *para*-(N–π–N) substituted **BIC-pCz** are diminished in both absorption and emission processes. Furthermore, **BIC-pCz** exhibits significant solvatochromism, with pronounced changes in its emission center and linewidth as a function of solvent polarity (Fig. S2 and Table S1†). In contrast, **BIC-mCz**, **mDBIC**, and **pDBIC** display no more significant solvent dependence in their emission spectra than the MR core, **BIC**. A redshifted emission with a sharper linewidth (λ_{em} = 536 nm, PL FWHM = 30 nm or 1037 cm^{-1}) is observed in **pDBIC** compared to its **BIC** core (λ_{em} = 439 nm, PL FWHM = 29 nm or 1482 cm^{-1}). Besides, all modified MR emitters except **pDBIC** exhibit delayed fluorescence properties in 2 wt%-doped mCP films. The corresponding photophysical parameters are

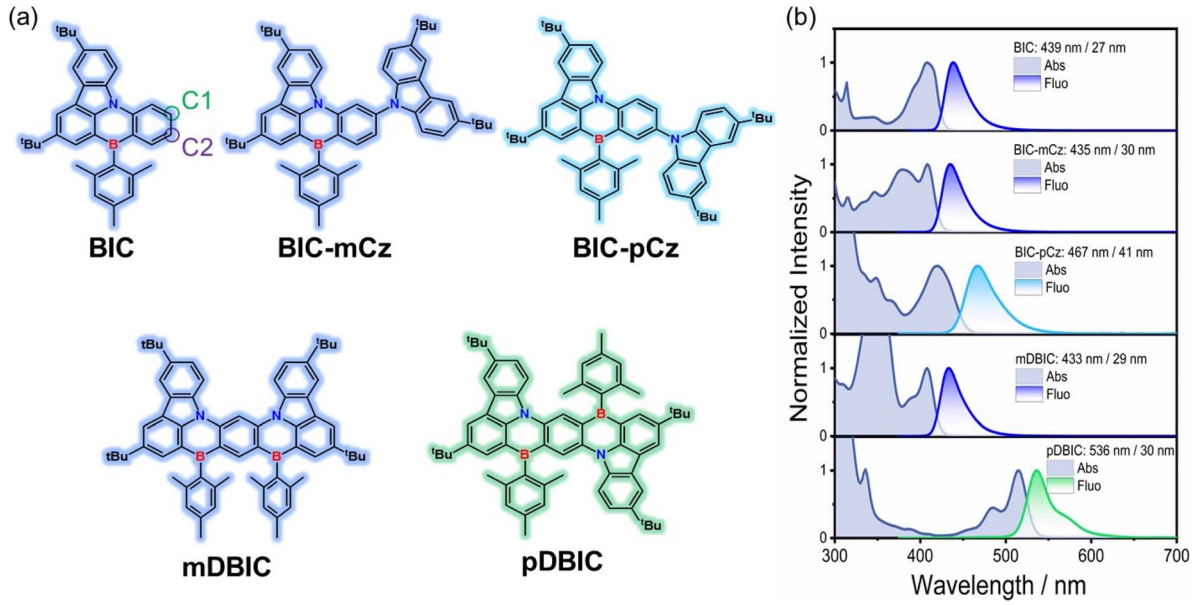

Fig. 2 (a) Chemical structures of BIC and its derivatives, with shadow colors approximately corresponding to the fluorescence emission colors of each compound. (b) Normalized stationary absorption and fluorescence spectra of BIC and its derivatives in toluene. The emission wavelength and FWHM are indicated on the fluorescence spectra. Fluorescence spectra were measured under excitation at 360 nm.

presented in Table S2.† In electroluminescence (EL), the emission spectra exhibit slight broadening and the FWHM of **BIC-mCz**, **BIC-pCz**, **mDBIC** and **pDBIC** is 42, 48, 42 and 30 nm, respectively (Table S3†).

Based on the above steady-state spectral characteristics, we here preliminarily establish the following trends regarding the site effects on color tuning: (1) the *meta*-(N–π–N) configuration promotes a blueshift, applicable to both peripheral modification and skeleton fusion; (2) the *para*-(N–π–N) configuration promotes a redshift in skeleton fusion, while the emission redshift in peripheral modification is achieved at the expense of narrowband emission properties. To fully understand the color tuning mechanism in MR-TADF emitters, we thus mainly consider the following three aspects: (1) the inheritance and regulation of the original MR characteristics through peripheral modification and skeleton fusion, (2) the influence of flexible EDG introduction at different sites of the MR skeleton on the transition nature of the lowest emission state, and (3) the structural rearrangement in the excited states and its impact on the electron-vibrational coupling and emission linewidth. To understand the importance of these factors, we thus utilize electronic excitation analysis to understand the preservation and modification of MR characteristics, as well as time-resolved spectroscopy to directly characterize the stabilization process of the lowest excited state and the accompanying energy loss.

Frontier molecular orbitals and transition analysis

The MR effect of the B/N skeleton leads to the formation of non-bonding frontier molecular orbitals (FMOs), which effectively reduce vibronic coupling and vibrational relaxation in the excited-state relaxation. This, in turn, facilitates the realization of highly efficient and narrowband emission. FMO and electron excitation analysis based on density functional theory (DFT) and time-dependent DFT (TD-DFT) provides simple and intuitive insight into the MR effect and the transition characteristics of the lowest excited states when discussing the peripheral modification and skeleton fusion expansion.

As shown in Fig. 3, the lowest unoccupied molecular orbital (LUMO) of the MR skeleton core, **BIC**, exhibits remarkable nonbonding characteristics, with electron density primarily localized on the boron atom and its *ortho* and *para* positions. The highest occupied molecular orbital (HOMO) is distributed on the nitrogen atoms, and exhibits delocalization over the PAH skeleton. The electron–hole analysis of the $S_0 \rightarrow S_1$ transition, which is predominantly contributed by the HOMO → LUMO transition, also reveals typical SRCT excitation characteristics (see Section S3 in the ESI† for the detailed excitation analysis).

Our previous study demonstrated that when D and A moieties are connected at a void position, where the frontier orbitals from the donor and acceptor are not distributed, a blue-shifted emission is realized compared with the conjugated D–A isomer.[48] The mechanism is explained as follows: when the conjugative effect is highly suppressed, the originally weaker inductive effect between D and A groups becomes dominant, causing the HOMO energy level to decrease and the LUMO energy level to rise, facilitating a larger energy gap in the D–void–A motif. Herein, **BIC-mCz** and **BIC-pCz** were designed by modifying the BIC core at the C1 and C2 positions. Given that **TCz** acts as an electron donor in these **BIC** derivatives, we focus

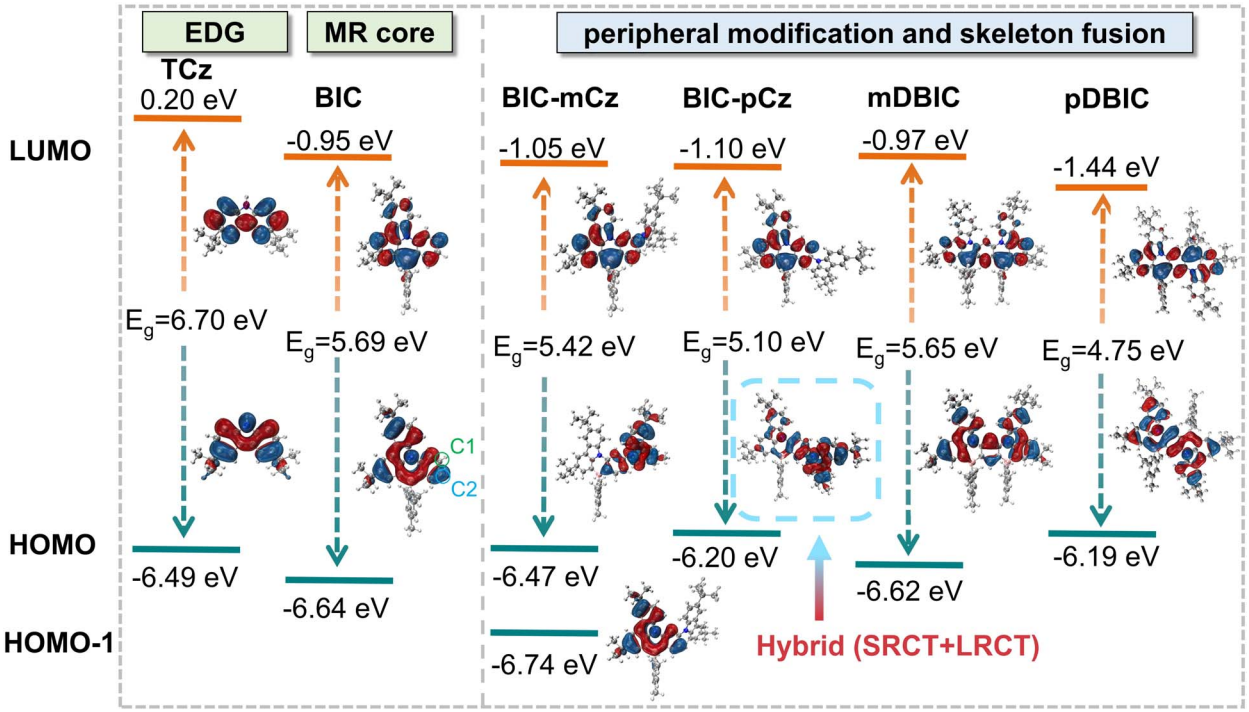

Fig. 3 Frontier molecular orbital (FMO) diagrams of BIC and its derivatives. Calculations were performed at the theoretical level of TD-M062X/6-31G(d,p) at their optimized S_0 geometries.

on the distributions and energies of HOMOs after chemical modifications. Due to electron density regulation induced by the MR effect of the B/N skeleton, a significant difference in electron density is observed between the C1 (0.12%) and C2 (8.39%) positions in the HOMO of the **BIC** core (Fig. 3 and S8†), as quantified using the Mulliken population method[49] with cross terms equally divided by the basis functions in the 6-31(d,p) set. Consequently, the C1 position acts as an ideal void site, whereas the C2 positions act as a conjugative site in constructing TCz-modified derivatives.

When **TCz** was introduced on the **BIC** core with the C1 position (*meta*-position) to form **BIC-mCz**, there are negligible electron density overlaps in the C1 position of the HOMO, thereby forming a D–void–A motif. Although a new HOMO localized on the **TCz** moieties is introduced in **BIC-mCz**, excitation analysis indicates that the $S_0 \rightarrow S_1$ transition in **BIC-mCz** is predominantly contributed by the HOMO−1 → LUMO transition (Table S5†). The HOMO−1 (−6.74 eV) in **BIC-mCz** completely inherits the electron distribution characteristics of the HOMO (−6.64 eV) of **BIC**. As a result, the $S_0 \rightarrow S_1$ transition in **BIC-mCz** still exhibits typical $SRCT_{BIC}$ transition characteristics (see the electron–hole analysis in Section S3 in the ESI†) with slightly higher excitation energy (3.67 eV) compared with that of **BIC** (3.68 eV). These calculation results are consistent with the observed spectral blueshift in the steady-state spectra, which is attributed to the inductive effect in a D–void–A motif when the conjugative effect is suppressed.

In contrast, **BIC-pCz** is formed by introducing **TCz** on the **BIC** core at the C2 position (*para*-position). In this case, the electron density of **BIC** and **TCz** can be effectively overlapped in **BIC-pCz** to form a conjugated D–π–A motif. The strong conjugative effect introduces a new HOMO delocalized over the connected **BIC** and **TCz** skeleton. Natural transition orbital (NTO) analysis further indicates that the $S_0 \rightarrow S_1$ transition (3.43 eV) in **BIC-pCz** is mainly attributed to hybrid $SRCT_{BIC}/LRCT_{TCz \rightarrow BIC}$ characteristics (Fig. S5†). From the perspective of color tuning, the peripheral modification at the conjugative site (*i.e.* the *para*-(N–π–N) configuration), realizes a redshift in the transition energy.

Furthermore, similar results and detailed theoretical analysis were also reported in other studies.[50,51] ***m*-Cz-BNCz** and ***p*-Cz-BNCz** are formed by respectively introducing the **TCz** into *meta*-/*para*-positions of boron in a blue MR core, **BNCz**. Due to the change in HOMO and LUMO distributions, ***p*-Cz-BNCz** exhibits identical HOMO and LUMO distributions and similar energy levels to **BNCz**, suggesting that *p*-substitution of **TCz** has negligible influence on the emission properties of **BNCz**. As a result, ***p*-Cz-BNCz** exhibits blue-shifted emission compared to **BNCz**. In contrast, the introduction of **TCz** at the *meta*-position of boron in **BNCz** results in the HOMO of ***m*-Cz-BNCz** being formed by the direct combination of the HOMOs of **BNCz** and **TCz**. The HOMO energy level of ***m*-Cz-BNCz** exhibits a remarkable increase, thereby suggesting a notable red-shift of the emission (λ_{em} = 519 nm, green emission).

For isomers **mDBIC** and **pDBIC** constructed with skeleton fusion, the fusion sites in a manner are analogous to those in the previous discussion, where **mDBIC**, with the *meta*-(N–π–N) configuration, can be viewed as an extended D–void–A fusion motif, and **pDBIC**, with the *para*-(N–π–N) configuration, can be considered an extended D–π–A fusion motif. As expected, the HOMO and LUMO of **mDBIC** both exhibit clear nonbonding characteristics. Although the orbitals become delocalized over the entire extended skeleton, the calculated HOMO–LUMO energy gap of **mDBIC** remains essentially unchanged compared to that of the **BIC** core. In the case of **pDBIC**, π-electron bonding characteristics are partially observed in both the HOMO and LUMO, particularly at the *para*-(N–π–N) and *para*-(B-π-B) position of the central phenyl. The HOMO–LUMO energy gap of **pDBIC** is accordingly minimized compared to that of the **BIC** core.

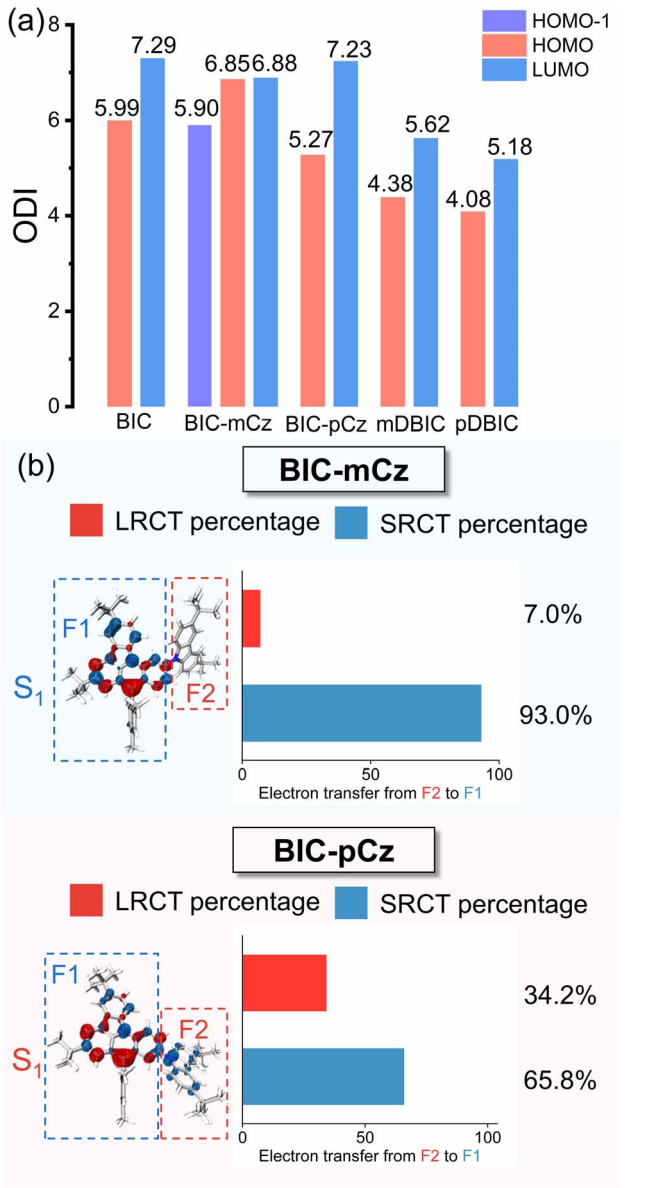

Fig. 4 (a) The orbital delocalization index (ODI) analysis of **BIC** and its derivatives. (b) Hole–electron distributions (hole: blue; electron: red) with inter-fragment charge-transfer (IFCT) analysis of (a) **BIC-mCz** and (b) **BIC-pCz**, respectively. **BIC-mCz** and **BIC-pCz** are divided into two fragments, *i.e.* F1 (B/N skeleton unit) and F2 (3,6-di-*tert*-butylcarbazole). All calculations at optimized S_0 geometries.

Electron distribution regulation by site-specific peripheral modifications

Skeleton modifications of B/N emitters for color tuning result in changes in the π-electron delocalization at the molecular level. The orbital delocalization index (ODI) is used to quantify the extent of orbital spatial delocalization, and the ODI value of orbital i is defined as:

$$\mathrm{ODI}_i = 0.01 \times \sum_A (\Theta_{A,i})^2$$

where $\Theta_{A,i}$ is the composition of atom A in orbital i. The ODI value ranges from 0 to 100, with lower values indicating a higher degree of orbital delocalization.[52] As shown in Fig. 4a, ODI values of HOMO−1 (5.90) and the LUMO (6.88) of **BIC-mCz** (noted that the $S_0 \rightarrow S_1$ transition in **BIC-mCz** is predominantly contributed by the HOMO−1 → LUMO transition) are essentially unchanged compared to that of the HOMO (5.99) and LUMO (7.29) of the **BIC** core. In contrast, the HOMO of **BIC-pCz** exhibits an enhanced orbital delocalization with the ODI reduced to 5.27. Meanwhile, the calculation results of nucleus-independent chemical shifts (NICSs), which indicate the aromaticity and delocalization of compounds, also suggest a larger π-electron delocalization in **BIC-pCz** (lower NICS value at the benzene ring in **BIC-pCz**) (Fig. S9†). Therefore, in site-specific peripheral modifications, the difference in **TCz**'s orbital involved in the $S_0 \rightarrow S_1$ transition results in different extents of FMO delocalization.

The interfragment charge-transfer (IFCT) analysis of the $S_0 \rightarrow S_1$ transition in **BIC-mCz** and **BIC-pCz** is used to further quantify the contributions of SRCT and LRCT (see Fig. 4b for fragment partitioning and IFCT results). In **BIC-mCz**, both the hole and electron distributions are localized on the F1 fragment, exhibiting dominant $\mathrm{SRCT_{BIC}}$ characteristics. In contrast, in **BIC-pCz**, the hole distribution is significantly delocalized across both the F1 and F2 fragments, demonstrating hybrid $\mathrm{SRCT_{BIC}/LRCT_{TCz\rightarrow BIC}}$ characteristics. The IFCT analysis reveals that the contribution of LRCT to the $S_0 \rightarrow S_1$ transition in **BIC-pCz** increases to 34.2%, compared to only 7.0% in **BIC-mCz**. Therefore, the D–void–A motif with a *meta*-(N–π–N) configuration is not expected to undergo significant structural rearrangement due to the flexibility of the peripheral EDG, achieving a blue-shifted narrowband emission. The D–π–A motif with a *para*-(N–π–N) configuration, while achieving a red-shifted emission, may experience emission broadening in dielectric environments due to the contribution of LRCT.

Electron distribution regulation by site-specific skeleton fusion

mDBIC and **pDBIC** are isomers constructed by fusing dual **BIC** moieties with *meta*- and *para*-(N–π–N) conjugations, respectively. Compared to the peripheral-modified emitters **BIC-mCz** and **BIC-pCz**, both **mDBIC** and **pDBIC** exhibit high rigidity in their extended skeletons. As a result, the ODI values of the FMOs for **mDBIC** and **pDBIC** indicate that the fusion of the skeleton significantly enhances π-electron delocalization (Fig. 4a). Hole-particle distributions of the $S_0 \rightarrow S_1$ transition also manifest SRCT characteristics, indicating that **TCz** has been fully integrated into the molecular skeleton, and the entire molecular structure no longer distinctly separates the electron donor and acceptor segments (Fig. S6 and S7†).

As mentioned above, the *para*-(N–π–N) configuration presents an extended D–π–A fusion motif, which introduces π-electron bonding characteristics and reduces the MR characteristics. These properties are clearly identified by the natural bonding orbital (NBO) and natural atomic orbital (NAO) analysis (see Fig. 5 and Table S9†). It is found that the π-electrons of **mDBIC** (*meta*-(N–π–N) conjugation) are localized on the atom, exhibiting non-bonding features. In contrast, the π-electrons of **pDBIC** (*para*-(N–π–N) conjugation) are localized on the atom and bond, exhibiting more bonding features (especially in the central benzene ring). Therefore, the MR characteristics are maintained or even enhanced in **mDBIC**, while the MR characteristics in **pDBIC** are reduced, leading to an emission shoulder at 570 nm (Fig. 2b).

It should be noted that, only **pDBIC** is centrosymmetric from the perspective of the molecular structure, and structural simulations also show that its central backbone is nearly planar (Fig. S14†). The electron–hole centroid distance of **pDBIC** is estimated to be about 0.079 Å, much lower than that of other emitters including its mirror symmetric isomer, **mDBIC** (1.134 Å) (Fig. S15†). Therefore, **pDBIC** combines the advantages of a highly rigid backbone and a near-zero intrinsic electric dipole moment, which helps suppress emission broadening in dielectric environments, thereby compensating for the

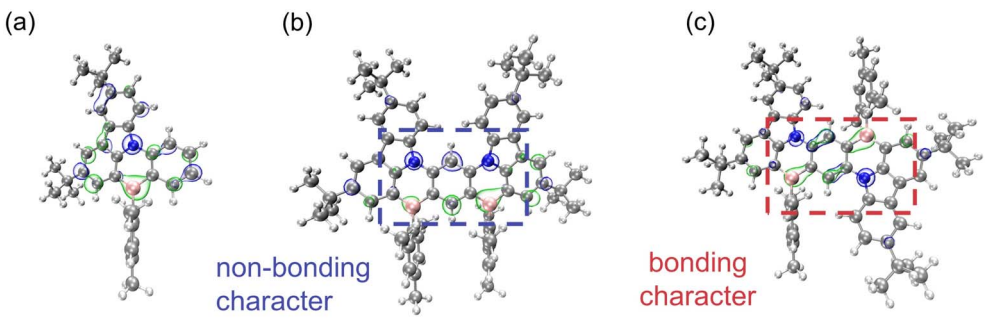

Fig. 5 The natural bonding orbital (NBO) analysis of (a) **BIC**, (b) **mDBIC** and (c) **pDBIC** in S_0 geometries. The blue and green bubbles represent the HOMO and LUMO contribution, respectively.

potentially increased electron-vibration coupling caused by the decline in MR properties in the *para*-(N–π–N) conjugation.

Structural flexibility and vibronic coupling on skeleton modification

From the perspective of electron distribution in frontier orbitals, emission redshift modulation *via* *para*-(N–π–N) modification is inevitably accompanied by a reduction in nonbonding characteristics (*i.e.* MR characteristics). However, the final emission linewidth of the MR-TADF emitter is determined by excited-state structural rearrangements and vibronic coupling of the emission transition, when environmental effects and intermolecular interactions are not considered.

The root-mean-square displacement (RMSD) values provide an appropriate and convenient approach to quantify the overall structural change between the optimized geometries of the S_0 and S_1 states (Table 1 and Fig. S16†). For **BIC-mCz**, despite containing a flexible peripheral EDG, the enhanced MR characteristics in the *meta*-(N–π–N) configuration lead to a suppression of structural rearrangement in the S_1 state with an RMSD value of 0.16 Å, compared to its **BIC** core (0.17 Å). In contrast, **BIC-pCz** exhibits a significantly larger excited-state structural rearrangement (0.42 Å). When examining the dihedral angle between the **BIC** core and TCz, **BIC-mCz** exhibits an increase in the dihedral angle from 43° in the optimized S_0 geometry to 46° in the S_1 geometry (Fig. S11†), suggesting a decoupling of **TCz** and the **BIC** core. This trend supports the proposed inhibition of the conjugation effect by the D–void–A motif. In contrast, **BIC-pCz** with a D–π–A motif exhibits a reduced dihedral angle as expected from 38.2° to 24.7° (Fig. S12†), indicating a significant enhancement of conjugation in the excited state, which facilitates the $^1LRCT_{TCz\rightarrow BIC}$ state involved in the emission transition.

We must note that structural relaxation is inhibited for emitters with fused skeletons, **mDBIC** and **pDBIC**, with root-mean-square displacement (RMSD) values of 0.24 and 0.08 Å, respectively (Table 1 and Fig. S16†). The dihedral angle changes between two fused **BIC** moieties were also negligible (Fig. S13 and S14†). The results about structural rearrangement indicate that extending PAH skeletons enhances the structural rigidity, while the D–void–A fusion motif, although constructed with flexible peripheral modification, also suppresses the excited-state structural rearrangement.

Table 1 Root-Mean-Square Displacement (RMSD) values, reorganization energy, and differences in the intramolecular dihedral angle between the B–N skeleton unit and TCz of BIC derivatives between the S_0 and S_1 states

Compound	RMSD [Å]	λ [eV]	$\theta_{S_1}-\theta_{S_0}$/[°]
BIC	0.17	0.21	NA
BIC-mCz	0.16	0.19	3.34
BIC-pCz	0.42	0.33	−13.47
mDBIC	0.24	0.18	2.29
pDBIC	0.08	0.16	0.35

Except for **BIC-pCz**, the **BIC** derivatives exhibit low reorganization energies between the S_0 and S_1 states, approximately 0.2 eV (Tables 1 and S11†), which facilitate narrow bandwidth emission and lead to a suppression of non-radiative decay

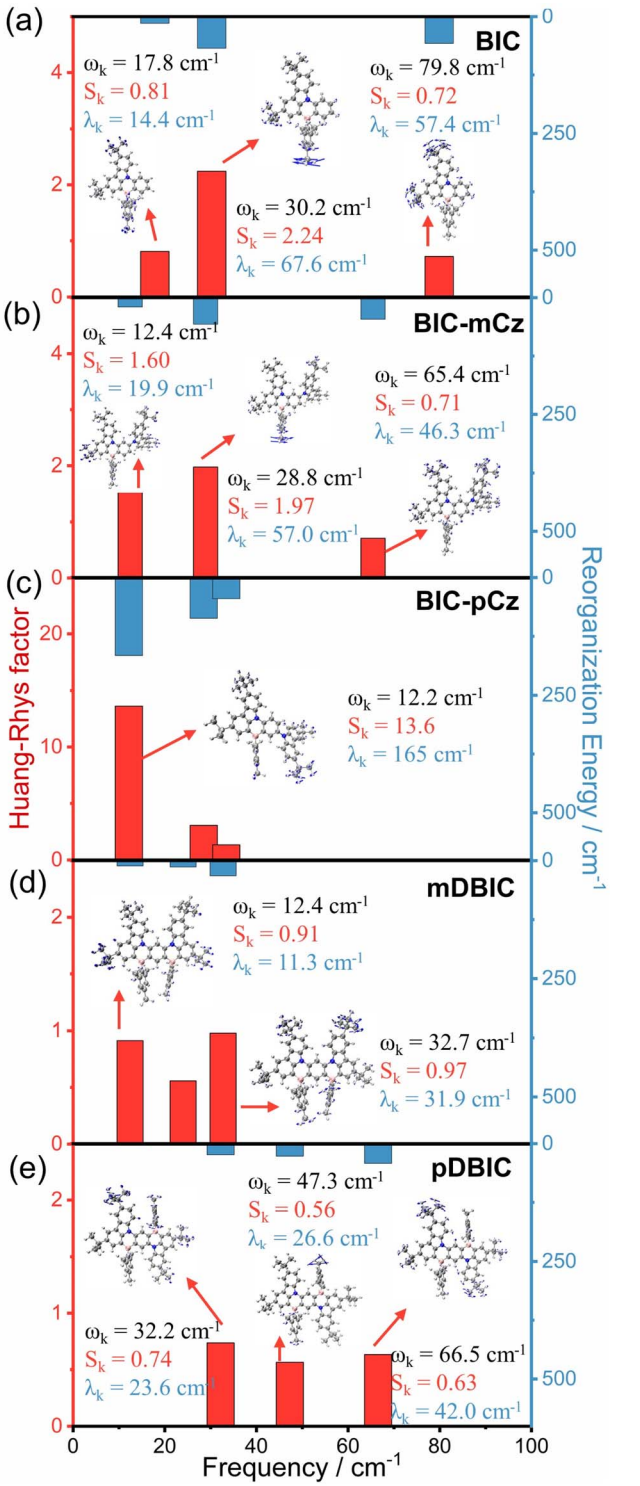

Fig. 6 The Huang–Rhys factor (S_k) and reorganization energy contribution (λ_k) of the first three major vibrational modes of (a) **BIC**, (b) **BIC-mCz**, (c) **BIC-pCz**, (d) **mDBIC** and (e) **pDBIC** for the $S_1 \rightarrow S_0$ transition in low frequency regions.

processes.[44,53–58] In this case, the contribution of specific vibrational modes to excited-state structural rearrangements and vibronic coupling during emission transitions could be considered. Vibrational modes with a considerable Huang–Rhys factor (S_k) will be strongly involved in the $S_0 \rightarrow S_1$ electronic transitions, while the λ_k is associated with either excited-state structural relaxation or the vibrational motion of the S_1 state, which broadens the emission linewidth. As shown in Fig. 6, **BIC-pCz** shows a dominant low-frequency vibrational mode ($\omega_k = 12.2\ cm^{-1}$) with an exceptionally large S_k (13.6) and λ_k (165 cm^{-1}), which is attributed to the dihedral motion between the **BIC** and *para*-(N–π–N) substituted **TCz** moieties. In contrast, the major vibrational models in the low-frequency range of the **BIC** core, *meta*-(N–π–N) substituted **BIC-mCz** and **mDBIC**, and *para*-(N–π–N) substituted **pDBIC** all exhibit small S_k and λ_k. Additionally, **pDBIC** shows better suppression of high-frequency modes (2500 to 3500 cm^{-1}) compared to its isomer, **mDBIC** (Fig. S18†). Notably, **pDBIC** exhibits distinct vibrational modes in the 1200–1500 cm^{-1} range (Fig. S18†), attributed to B/N-embedded acene skeleton stretching vibrations, a feature absent in the other four MR emitters. These modes contribute significantly to its emission profile, likely accounting for the shoulder peak observed in its spectrum.

Therefore, we deduce that for the two emitters regulated in the direction of the long wavelength with *para*-(N–π–N) configurations, peripheral-modification constructed **BIC-pCz** may exhibit significant excited-state relaxation, while **pDBIC**, with a centrosymmetric rigid skeleton, may undergo minimal structural relaxation. Furthermore, the SOC constant between the S_1 and T_1 state ($\langle S_1|\hat{H}_{SOC}|T_1\rangle$) in **BIC-pCz**, due to the mixing LRCT characteristics in the S_1 state, is significantly enhanced (0.31 cm^{-1}) compared with that of other MR emitters (Fig. S20†).

Excited-state structural rearrangement in skeleton modifications revealed by time-resolved spectroscopy

Femtosecond transient absorption (fs-TA) spectroscopy is further employed to gain dynamic insights into the structural relaxation processes of peripheral modification and skeleton fusion,[59,60] particularly for **BIC** derivatives with flexible EDG modifications. Fig. 7 shows the representative fs-TA spectra of **BIC**, **BIC-mCz**, and **BIC-pCz** in dichloromethane (DCM). The excitation wavelengths were set to 385 nm for **BIC** and **BIC-mCz**, and 405 nm for **BIC-pCz**, selectively exciting the low-lying ^{1}SRCT states and mixed ^{1}SRCT/^{1}LRCT states, respectively. For the MR core, **BIC** (Fig. 7a), the initial spectrum at 0.21 ps after photoexcitation shows a positive excited-state absorption (ESA) signal between 500 and 750 nm, which overlaps with the negative ground-state bleach (GSB) below 400 nm and negative stimulated emission (SE) at around 450 nm, as identified by the corresponding steady-state absorption and emission spectra. Following a slight redshift of the SE band by around 7 nm over a few picoseconds, the spectral profile remains stable on a nanosecond scale, until a long-lived species develops. Global spectral analysis (lower panels in Fig. 7) based on a sequential evolution model in the 7 ns time window helps us evaluate the spectral evolution. The rapid stabilization of the SE band indicates a very limited excited-state structural rearrangement in the rigid **BIC** skeleton.[14,41] The long-lived species is identified as the ^{3}SRCT state based on nanosecond transient absorption (ns-TA) spectroscopy under nitrogen-purged conditions (Fig. S25 and S28†).

We compare the initial spectral evolution of the four **BIC** derivatives, focusing on the dynamics of structural rearrangement. As expected, the two compounds constructed by skeleton fusion, **mDBIC** and **pDBIC** (Fig. S21†), exhibit very minimal SE evolution. This is consistent with the minimal Stokes shift and

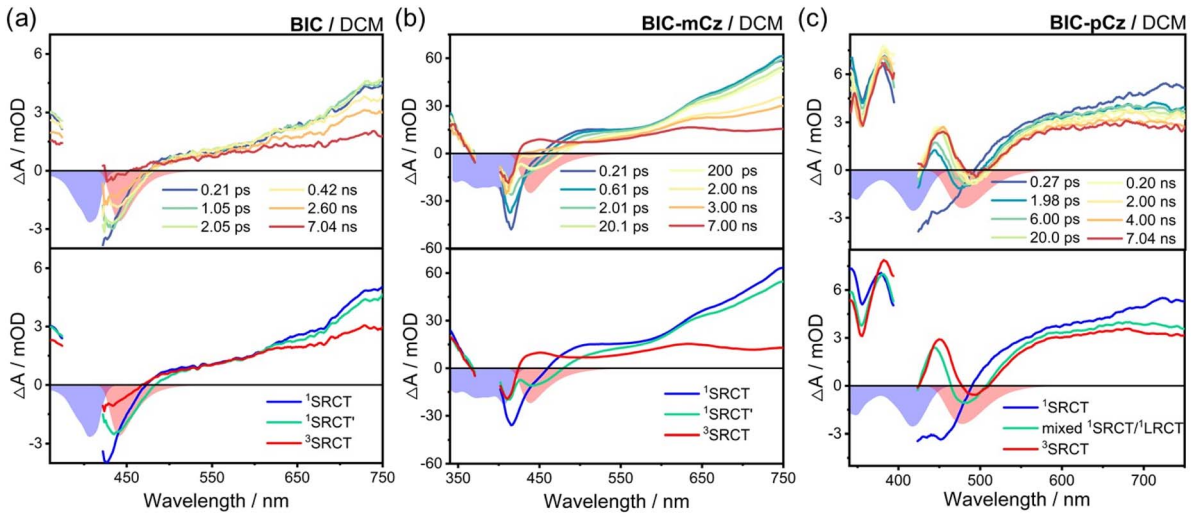

Fig. 7 Representative fs-TA spectra of (a) **BIC** (λ_{ex} = 385 nm); (b) **BIC-mCz** (λ_{ex} = 385 nm), and (c) **BIC-pCz** (λ_{ex} = 405 nm) in DCM. Evolution-associated different spectra (EADS) obtained from the global analysis based on a sequential evolution model are shown in the lower panel of the corresponding TA spectra in the 7 ns time window. The fitting time constants are shown in Table S12.† The blue and red shaded areas represent the corresponding steady-state absorption and emission spectra, respectively. SRCT: short-range charge-transfer state, SRCT′: structurally relaxed short-range charge-transfer state, and LRCT: long-range charge-transfer state.

narrowband emission observed in their steady-state spectra. This can be undoubtedly attributed to excellent skeleton rigidity by the EDG fusion in the BIC parent. For **BIC-mCz** and **BIC-pCz**, while both feature a flexible peripheral EDG and share the same **BIC** core, they exhibit different degrees of SE evolution. As indicated in the electron excitation analysis, peripheral modification in the *meta*-(N–π–N) configuration does not induce significant π-electron delocalization. Consequently, the electron density of the EDG in **BIC-mCz** is not involved in the emission transition. The emission transition that retained or even enhanced MR characteristics shows minimal sensitivity to solvent polarity. Therefore, the flexible EDG modifications in the *meta*-(N–π–N) configuration do not result in additional excited state structural rearrangement. In contrast, flexible EDG modification in the *para*-(N–π–N) configuration (*i.e.* **BIC-pCz**) leads to the bonding characteristics at the C–N connection site between the **BIC** core and the carbazole moiety, and accordingly the MR characteristics are reduced. The π-electron delocalization stabilizes the LRCT state, which replaces the original SRCT state of the **BIC** core and becomes the lowest emissive state. A sizable electric dipole moment in the S_1 state results in a remarkable solute–solvent interaction. Therefore, we observe significant SE evolution in central wavelength and intensity, which suggests a substantial excited-state structural rearrangement in the solvent environment, even in weakly polar toluene (Fig. S22†). The proposed excited state relaxation mechanism of **BIC** derivatives is summarized in Fig. S30.†

Conclusions

In this study, two sets of peripheral modification and skeleton fusion B/N-skeleton isomers have been investigated as proof-of-concept models to thoroughly demonstrate the site effects in the color-tuning mechanism of MR-TADF emitters. Due to the atomically separated frontier orbital distribution of the core B/N skeleton, the *meta*-(N–π–N) peripheral modification forms a D–void–A motif *via* facilitating the inductive effect and suppressing the conjugative effect, leading to a blue-shift in emission. Meanwhile, LRCT character is prevented from participating in the emission process and thereby maintaining the characteristics of the narrowband emission. This strategy is also applicable to *meta*-(N–π–N) skeleton extension, which can be viewed as an extended D–void–A motif. For the *para*-(N–π–N) configuration, the D–π–A motif is formed *via* a strong conjugative effect and π-electron delocalization, leading to a red-shift in emission. Although the conjugative effect reduces the original non-bonding MR properties, excellent narrowband green emission (**pDBIC**, 528 nm, 30 nm or 929 cm^{-1} in emission FWHM) is achieved by skeleton fusion of dual **BIC** in the *para*-(N–π–N) configuration. The rigid centrosymmetric backbone compensates for the potentially increased vibronic coupling caused by the decline in MR properties and further suppresses the emission broadening in dielectric environments induced by the excited-state structural relaxation. Elucidating the site effects in the color-tuning mechanism in B/N-skeleton MR-TADF emitters is poised to make contributions in the following areas: (i) maintaining and enhancing MR characteristics through multiple fusion skeletons or large skeleton extensions;[22] (ii) fine-tuning of emission colors *via* skeletal modifications while suppressing the emission broadening induced by vibronic coupling or excited-state structural relaxation,[18] and (iii) addressing the molecular design challenge of achieving ultra-pure three primary colors,[37,61] thus paving the way for future advancements of OLED materials.

Data availability

The data supporting this article have been included within the article or as part of the ESI.†

Author contributions

Z. S.: conceptualization, methodology, investigation, data curation, formal analysis, visualization, and writing – original draft; X. L. and S. W.: data curation, formal analysis, and validation; X. W.: resources; Y. L. and Y. W.: data curation and methodology: L. D.: resources and supervision; A. X.: supervision, resources, and funding acquisition; Z. K.: conceptualization, funding acquisition, supervision, and writing – review and editing.

Conflicts of interest

There are no conflicts to declare.

Acknowledgements

This work was supported by the National Natural Science Foundation of China (NSFCs, Grant No. 22303008, 22133001, and 22203009), the Beijing Natural Science Foundation (Grant No. 2232012), and the BUPT Excellent Ph.D. Students Foundation (Grant No. CX2023109).

Notes and references

1 T. Hatakeyama, K. Shiren, K. Nakajima, S. Nomura, S. Nakatsuka, K. Kinoshita, J. Ni, Y. Ono and T. Ikuta, *Adv. Mater.*, 2016, **28**, 2777–2781.
2 S. Madayanad Suresh, D. Hall, D. Beljonne, Y. Olivier and E. Zysman-Colman, *Adv. Funct. Mater.*, 2020, **30**, 1908677.
3 H. J. Kim and T. Yasuda, *Adv. Opt. Mater.*, 2022, **10**, 2201714.
4 K. R. Naveen, H. I. Yang and J. H. Kwon, *Commun. Chem.*, 2022, **5**, 149.
5 K. R. Naveen, P. Palanisamy, M. Y. Chae and J. H. Kwon, *Chem. Commun.*, 2023, **59**, 3685–3702.
6 Y. Xu, Q. Wang, X. Cai, C. Li, S. Jiang and Y. Wang, *Angew. Chem., Int. Ed.*, 2023, **62**, e202312451.
7 M. Mamada, M. Hayakawa, J. Ochi and T. Hatakeyama, *Chem. Soc. Rev.*, 2024, **53**, 1624–1692.
8 G. Hong, X. Gan, C. Leonhardt, Z. Zhang, J. Seibert, J. M. Busch and S. Bräse, *Adv. Mater.*, 2021, **33**, 2005630.
9 X. Liang, Z.-P. Yan, H.-B. Han, Z.-G. Wu, Y.-X. Zheng, H. Meng, J.-L. Zuo and W. Huang, *Angew. Chem., Int. Ed.*, 2018, **57**, 11316–11320.

10 Y. Xu, C. Li, Z. Li, J. Wang, J. Xue, Q. Wang, X. Cai and Y. Wang, *CCS Chem.*, 2021, **4**, 2065–2079.
11 Z. Huang, H. Xie, J. Miao, Y. Wei, Y. Zou, T. Hua, X. Cao and C. Yang, *J. Am. Chem. Soc.*, 2023, **145**, 12550–12560.
12 J.-M. Jin, D. Liu, W.-C. Chen, C. Shi, G. Chen, X. Wang, L. Xing, W. Ying, S. Ji, Y. Huo and S.-J. Su, *Angew. Chem., Int. Ed.*, 2024, **63**, e202401120.
13 Q.-Y. Meng, X.-L. Wen and J. Qiao, *J. Phys. Chem. Lett.*, 2024, **15**, 12571–12583.
14 Z. Situ, X. Li, H. Gao, J. Zhang, Y. Li, F. Zhao, J. Kong, H. Zhao, M. Zhou, Y. Wang, Z. Kuang and A. Xia, *J. Phys. Chem. Lett.*, 2024, **15**, 4197–4205.
15 R. Zhong, M. Wang, X. Wang, S. Wang, S. Shao and L. Wang, *Chem. Sci.*, 2024, **15**, 13290–13298.
16 Y. Zou, M. Yu, Y. Xu, Z. Xiao, X. Song, Y. Hu, Z. Xu, C. Zhong, J. He, X. Cao, K. Li, J. Miao and C. Yang, *Chem*, 2024, **10**, 1485–1501.
17 R. K. Konidena, M. Yang and T. Yasuda, *Chem. Commun.*, 2023, **59**, 10251–10254.
18 L. Ge, W. Zhang, Y.-H. Hao, M. Li, Y. Liu, M. Zhou and L.-S. Cui, *J. Am. Chem. Soc.*, 2024, **146**, 32826–32836.
19 Y. Kondo, K. Yoshiura, S. Kitera, H. Nishi, S. Oda, H. Gotoh, Y. Sasada, M. Yanai and T. Hatakeyama, *Nat. Photonics*, 2019, **13**, 678–682.
20 M. Yang, I. S. Park and T. Yasuda, *J. Am. Chem. Soc.*, 2020, **142**, 19468–19472.
21 Y. Sano, T. Shintani, M. Hayakawa, S. Oda, M. Kondo, T. Matsushita and T. Hatakeyama, *J. Am. Chem. Soc.*, 2023, **145**, 11504–11511.
22 T. Hua, X. Cao, J. Miao, X. Yin, Z. Chen, Z. Huang and C. Yang, *Nat. Photonics*, 2024, **18**, 1161–1169.
23 K. R. Naveen, J. H. Oh, H. S. Lee and J. H. Kwon, *Angew. Chem., Int. Ed.*, 2023, **62**, e202306768.
24 S. Wu, W. Li, K. Yoshida, D. Hall, S. Madayanad Suresh, T. Sayner, J. Gong, D. Beljonne, Y. Olivier, I. D. W. Samuel and E. Zysman-Colman, *ACS Appl. Mater. Interfaces*, 2022, **14**, 22341–22352.
25 J. M. dos Santos, C.-Y. Chan, S. Tang, D. Hall, T. Matulaitis, D. B. Cordes, A. M. Z. Slawin, Y. Tsuchiya, L. Edman, C. Adachi, Y. Olivier and E. Zysman-Colman, *J. Mater. Chem. C*, 2023, **11**, 8263–8273.
26 Y. Zhang, D. Zhang, J. Wei, Z. Liu, Y. Lu and L. Duan, *Angew. Chem., Int. Ed.*, 2019, **58**, 16912–16917.
27 H. Gao, Z. Li, Z. Pang, Y. Qin, G. Liu, T. Gao, X. Dong, S. Shen, X. Xie, P. Wang, C.-S. Lee and Y. Wang, *ACS Appl. Mater. Interfaces*, 2023, **15**, 5529–5537.
28 Y. Hu, J. Miao, C. Zhong, Y. Zeng, S. Gong, X. Cao, X. Zhou, Y. Gu and C. Yang, *Angew. Chem., Int. Ed.*, 2023, **62**, e202302478.
29 J. Jin, M. Chen, H. Jiang, B. Zhang, Z. Xie and W.-Y. Wong, *ACS Mater. Lett.*, 2024, **6**, 3246–3253.
30 L. Xing, J. Wang, W.-C. Chen, B. Liu, G. Chen, X. Wang, J.-H. Tan, S. S. Chen, J.-X. Chen, S. Ji, Z. Zhao, M.-C. Tang and Y. Huo, *Nat. Commun.*, 2024, **15**, 6175.
31 H. L. Lee, J. Kang, J. Lim, S. C. Kim, S. O. Jeon and J. Y. Lee, *Nat. Commun.*, 2023, **14**, 4818.
32 N. Ikeda, S. Oda, R. Matsumoto, M. Yoshioka, D. Fukushima, K. Yoshiura, N. Yasuda and T. Hatakeyama, *Adv. Mater.*, 2020, **32**, 2004072.
33 S. M. Suresh, E. Duda, D. Hall, Z. Yao, S. Bagnich, A. M. Z. Slawin, H. Bässler, D. Beljonne, M. Buck, Y. Olivier, A. Köhler and E. Zysman-Colman, *J. Am. Chem. Soc.*, 2020, **142**, 6588–6599.
34 I. S. Park, M. Yang, H. Shibata, N. Amanokura and T. Yasuda, *Adv. Mater.*, 2022, **34**, 2107951.
35 S. Xiao, X. Cao, G. Chen, X. Yin, Z. Chen, J. Miao and C. Yang, *Angew. Chem., Int. Ed.*, 2024, e202418348.
36 K. Xu, N. Li, Z. Ye, Y. Guo, Y. Wu, C. Gui, X. Yin, J. Miao, X. Cao and C. Yang, *Chem. Sci.*, 2024, **15**, 18076–18084.
37 W. Yuan, Q. Jin, M. Du, L. Duan and Y. Zhang, *Adv. Mater.*, 2024, **36**, 2410096.
38 M. Hayakawa, X. Tang, Y. Ueda, H. Eguchi, M. Kondo, S. Oda, X.-C. Fan, G. N. Iswara Lestanto, C. Adachi and T. Hatakeyama, *J. Am. Chem. Soc.*, 2024, **146**, 18331–18340.
39 K. Ye, G. Li, F. Li, C. Shi, Z. Jiang, F. Zhang, Q. Li, J. Su, D. Song and A. Yuan, *Phys. Chem. Chem. Phys.*, 2024, **26**, 2395–2401.
40 Z. Kuang, G. He, H. Song, X. Wang, Z. Hu, H. Sun, Y. Wan, Q. Guo and A. Xia, *J. Phys. Chem. C*, 2018, **122**, 3727–3737.
41 Y. Gao, Y. Wang, Z. Guo, Y. Wan, C. Li, B. Yang, W. Yang and X. Ma, *J. Phys. Chem. B*, 2022, **126**, 2729–2739.
42 X. Qian, F. Chu, W. Zhou, Z. Zheng, X. Chen and Y. Zhao, *J. Phys. Chem. Lett.*, 2023, **14**, 3335–3342.
43 X. Chen, L. Sun, A. A. Sukhanov, S. Doria, L. Bussotti, J. Zhao, H. Xu, B. Dick, V. K. Voronkova and M. Di Donato, *Chem. Sci.*, 2024, **15**, 10867–10881.
44 Y. Gao, Y. Wang, Z. Guo, Y. Wan, Z. Xue, Y. Han, W. Yang and X. Ma, *Chem. Sci.*, 2024, **15**, 6410–6420.
45 M. Lu, S. Liao, J. Li, Z. Yu, N. Zhao, Z. Xie, S. Chen, L. Dang and M.-D. Li, *Chin. Chem. Lett.*, 2024, 110066.
46 P. Li, W. Li, X. Wang, P. Zhang, Q. Lv, C. Sun, C. Yin and R. Chen, *J. Phys. Chem. Lett.*, 2025, **16**, 340–348.
47 X. Wang, Y. Zhang, H. Dai, G. Li, M. Liu, G. Meng, X. Zeng, T. Huang, L. Wang, Q. Peng, D. Yang, D. Ma, D. Zhang and L. Duan, *Angew. Chem., Int. Ed.*, 2022, **61**, e202206916.
48 D. Zhang, Y. Wada, Q. Wang, H. Dai, T. Fan, G. Meng, J. Wei, Y. Zhang, K. Suzuki, G. Li, L. Duan and H. Kaji, *Adv. Sci.*, 2022, **9**, 2106018.
49 T. Lu and F. Chen, *J. Comput. Chem.*, 2012, **33**, 580–592.
50 Y. Xu, C. Li, Z. Li, Q. Wang, X. Cai, J. Wei and Y. Wang, *Angew. Chem., Int. Ed.*, 2020, **59**, 17442–17446.
51 Z. Pei, Q. Ou, Y. Mao, J. Yang, A. d. l. Lande, F. Plasser, W. Liang, Z. Shuai and Y. Shao, *J. Phys. Chem. Lett.*, 2021, **12**, 2712–2720.
52 T. Lu, *J. Chem. Phys.*, 2024, **161**, 082503.
53 M. K. Etherington, J. Gibson, H. F. Higginbotham, T. J. Penfold and A. P. Monkman, *Nat. Commun.*, 2016, **7**, 13680.
54 Z. Wang, R. Jing, Y. Li, D. Song, Y. Wan, N. Fukui, H. Shinokubo, Z. Kuang and A. Xia, *J. Phys. Chem. Lett.*, 2023, **14**, 8485–8492.
55 P.-A. Yin, Q. Ou, Q. Peng and Z. Shuai, *Aggregate*, 2023, **4**, e291.

56 Z. Guo, Y. Zhu, A. Zhou, Y. Zhao, W. Nie, V. Utochnikova and H. Meng, *J. Phys. Chem. Lett.*, 2024, **15**, 11664–11670.
57 X. Li, Z. Kuang, Z. Situ, T. Huang, R. Jing, J. Kong, Y. Li, D. Song, M. Zhou, L. Duan and A. Xia, *J. Phys. Chem. C*, 2024, **128**, 6612–6620.
58 H. L. Lee, S. O. Jeon, I. Kim, S. C. Kim, J. Lim, J. Kim, S. Park, J. Chwae, W.-J. Son, H. Choi and J. Y. Lee, *Adv. Mater.*, 2022, **34**, 2202464.
59 X. Jin, S. Guo, X. Wang, M. Cong, J. Chen, Z. Zhang, J. Su, D.-H. Qu and H. Tian, *Angew. Chem., Int. Ed.*, 2023, **62**, e202305572.
60 K. Hu, X. He, P. Jin, X. Wang, H. Pan and J. Chen, *ChemPhotoChem*, 2024, **8**, e202400108.
61 J.-J. Hu, X. Liang, Z.-P. Yan, J.-Q. Liang, H.-X. Ni, L. Yuan, J.-L. Zuo and Y.-X. Zheng, *Angew. Chem., Int. Ed.*, 2025, e202421102.